ANALYSIS OF METHODS USED TO RECONSTRUCT THE FLIGHT PATH OF MALAYSIA AIRLINES FLIGHT 370

JOHN ZWECK*

1. Introduction. In the early hours of March 8, 2014, a Malaysia Airlines Boeing 777 disappeared en route from Kuala Lumpur to Beijing with 239 people on board [10]. At the time of writing this article there has been no confirmation of any debris from the aircraft and no survivors have been found. If the crash site is not discovered, this tragedy may become of one of the great aviation mysteries.

The disappearance of MH370 is all the more mysterious in the age of highly accurate global navigation and communications systems. During flight, commercial aircraft use satellite communications links to exchange information with ground stations via the Aircraft Communications Addressing and Reporting System (ACARS) [6]. Although most of the functionality of ACARS was disabled early in the flight, for six hours after the last radar contact the aircraft and ground station exchanged a series of short messages, which we will refer to as **pings**. These messages were relayed to a ground station in Perth, Australia, by the Inmarsat 3-F1 satellite which was in a geosynchronous orbit over the equator at longitude 64.5°E.

A team of engineers at the British satellite company Inmarsat discovered that for each ping, ACARS recorded three pieces of data: the ping time, the Burst Timing Offset (BTO), and the Burst Frequency Offset (BFO). The BFO, which is discussed in Section 3 below, is a quantity that is related to the Doppler shift due to the motion of the aircraft relative to the satellite. The BTO is a time delay measured at the ground station which the satellite engineers used to accurately determine the distance between the aircraft and the satellite at each ping time [2]. As we see in Figure 1.1, the set of all points on a sphere (the earth) that are at a fixed distance from a given point (the satellite) forms a circle. Therefore, factoring in the speed and fuel constraints of the aircraft, the satellite engineers determined that at the each ping time the aircraft was located somewhere on a segment of a circle, which we call a **ping arc**. Each such circle is characterized by a **ping arc angle**, which is the angle between the aircraft and the satellite, as measured from the center of the earth (see Figure 1.1). Consequently, they were able to deduce that at the last ping time, the aircraft was located somewhere on a ping arc that extended from the latitude of the Roaring Forties in the southern Indian Ocean to the steppes of Central Asia. We show the ping circles in Figure 1.2 (A), and in Table 1.1 we show the ping times, the ping arc angles (which can be computed from the BTO data [2]), and the BFO data.

The Doppler effect is a property of an electromagnetic signal that is due to the relative motion between a source (the aircraft) and a receiver (the satellite). If the distance between the aircraft and the satellite is decreasing then the frequency of the received signal will be higher than that of the transmitted signal, and if the distance is increasing the received frequency will be lower. This change in frequency is called the Doppler shift. The Doppler shift is proportional to the component of the relative velocity vector of the two moving objects that is in the direction of the displacement vector between them. Taken together, the BTO and BFO data provide partial position and velocity information for the aircraft at each of the ping times.

*Department of Mathematical Sciences, University of Texas at Dallas, 800 West Campbell Road, Richardson, TX 75080-3021 (zweck@utdallas.edu).

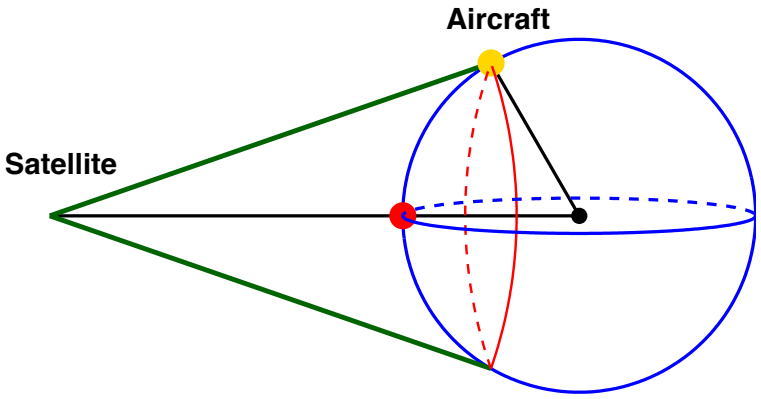

FIG. 1.1 *Sketch illustrating the circle (shown in red) whose points are at the same altitude above the surface of the earth and at the same distance from the satellite as the aircraft (shown with a yellow dot). The distance of the satellite from the center of the earth is 6.6 times the radius of the earth, whereas the altitude of the aircraft was approximately 10 km. (The radius is the earth is 6,370 km.) The red dot is the projection of the satellite onto the sphere of radius 6380 km.*

Although the ping data recorded by the ACARS system was not specifically designed to be used for tracking aircraft, the Inmarsat engineers rapidly developed mathematical methods to determine flight paths that best fit the BTO and BFO data. These flight paths were then used to identify search areas located on the last ping arc in the southeast Indian Ocean. Because of the urgency of the search for the aircraft's black boxes, the initial search areas were based on preliminary analyses of the satellite data. Since it took time to understand and analyze the satellite data and other relevant information, the search area was changed several times between March 9th and June 26th. While these changes in the search area presented a public relations challenge, they also gave the general public a rare opportunity to witness an engineering team attempt to solve a high profile research problem.

In this article, we describe mathematical models similar to those used by the government-appointed Satellite Working Group (SWG) to reconstruct the flight path of MH370 and presented in a June 26th, 2014 report by the Australian Transport Safety Bureau (ATSB) [2]. We will validate these models using data from simulated flight paths and by comparing the results we obtained for MH370 to those found by the SWG. We work analytically as much as possible and only resort to numerical methods when necessary. The exposition is aimed at students with a background in vector calculus, matrix analysis, and numerical analysis and who are at the transition between an undergraduate education in mathematics and a graduate education in mathematics or engineering. At the end of each section we have included a range of modeling, analytical, and numerical problems, some of which are open ended.[1]

We will develop a series of three progressively more realistic models. In Model I, we assume a known constant ground speed for the aircraft and we approximate the flight path by a concatenation of segments of great circles. With Model I, the satellite is assumed to be in a **geostationary orbit**, which means that from the point of view of an observer on the earth the satellite is always located at a fixed point in

[1]Solutions to selected starred problems$^{(*)}$ are provided in an Appendix in the online supplementary material.

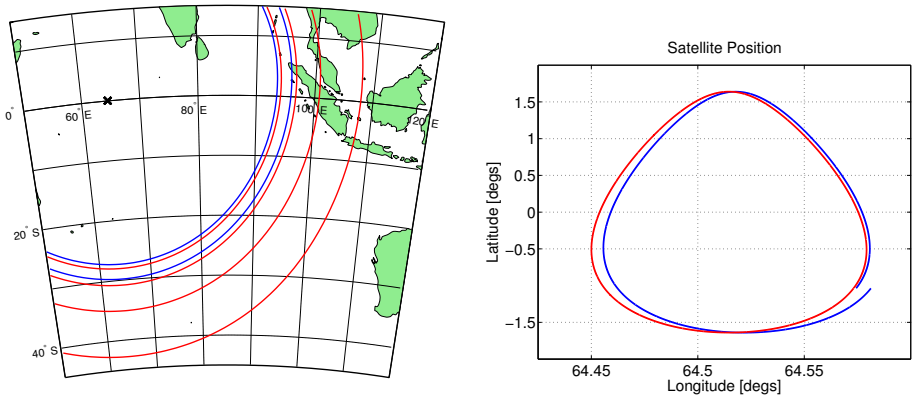

(A) (B)

FIG. 1.2 *(A) The ping arcs (blue and red curves) and the nominal location of the projection of the satellite onto the surface of the earth (black cross). The aircraft first crossed the two blue arcs traveling towards the black cross and then crossed the four red arcs traveling away from it. (B) The projection of the geosynchronous orbit of the Inmarsat 3-F1 satellite onto the surface of the earth. Red curve: model (see Section 4). Blue curve: data.*

TABLE 1.1 *The relevant satellite data [2], [4]. Times are given in Coordinated Universal Time (UTC) which is the successor to Greenwich Mean Time. At the time of last radar contact (18:15 UTC) the aircraft was located at* $97.72^\circ E$, $6.82^\circ N$.

Ping Time (UTC)	18:28	19:41	20:41	21:41	22:41	24:11
Ping Arc Angle, Φ [deg]	31.42	29.01	29.67	32.27	36.30	43.44
BFO [Hz]	143	111	141	168	204	252

the sky above the equator [9]. This model, which does not make use of the BFO data, is similar to that used between March 17th and April 1st to determine search areas for the missing aircraft [2]. A preliminary version of this model was discussed in [14]. In Model II, the flight path is approximated by a concatenation of segments of constant-speed great circles for which the different segments have *a priori* unknown speeds. This semi-analytical model makes use of aircraft-satellite Doppler shift data at the ping times. With Model II, the satellite is assumed to be in a **geosynchronous** orbit, which means that from the point of view of an observer on the earth the satellite returns to the same point in the sky at the same time each day. In particular, if the orbit is a constant speed, perfect circle in a plane that is slightly tilted with respect to the equator, then the motion of the satellite over the surface of the earth takes the form of a figure-eight curve [11]. However, in Section 4 we will see that in reality the Inmarsat 3-F1 satellite traces out a curve on the earth that looks more like a very narrow teardrop-shaped curve (see Figure 1.2 (B)). Finally, in Model III we develop a fully numerical model based on segments of small circles and which uses the recorded BFO data. For all three models, we assume that the earth is a perfect sphere and that the aircraft flies at a constant altitude, which we took to be 35,000 feet (10.7 km).

2. Model I: The Known-Speed, Concatenation-of-Geodesics Model. Inmarsat's initial attempts to reconstruct the flight path of MH370 from the ping data used the last known location of the aircraft, viable aircraft speeds, and trigonometry

to identify flight paths that crossed each of the ping arcs at the appropriate time. For these calculations, they assumed that the aircraft was "flying at a steady speed on a relatively constant track consistent with an aircraft operating without human control" [1]. The flight paths reconstructed by Inmarsat were then used by the ATSB to define initial search areas for the aircraft in the southern Indian Ocean. In this section, we describe a model that incorporates the main assumptions and ideas used by the Inmarsat engineering team.

In this model, we assume that the altitude of the aircraft is a known constant. Therefore, the flight path of the aircraft is constrained to lie on a sphere whose center is the center of mass of the earth and whose radius, R_A, is determined by the altitude of the aircraft. This sphere is depicted in Figure 2.1 (A). We also assume that the ground speed of the aircraft is a known constant, and we approximate the flight path by a concatenation of segments of great circles on the sphere. A **great circle** is the intersection of a sphere with a plane through the center of the sphere. The equator and circles of longitude are examples of great circles on the surface of the earth. The yellow and green curves in Figure 2.1 (A) are great circles. Segments of great circles on the sphere and straight lines in the plane are examples of **geodesics**, which are the constant speed curves on a surface (or more generally on a Riemannian manifold) that locally minimize the distance between two points on the surface [5].

The speed and initial position of the aircraft are input parameters to the model. Starting at a given initial position on the first ping arc, we need to find a great circle segment that ends on the second ping arc at the second ping time. Then, starting from the position we just reached on the second ping arc, we repeat the process—using a segment of a possibly different great circle—to reach the third ping arc at the third ping time, and so on. Note that with this model we make no attempt to match the Doppler shift (or BFO) data recorded at the ping times. For simplicity, we assume that the satellite is in a geostationary orbit at an altitude of 35,786 km above the point on the equator at longitude 64.5°E. Since a great circle through a given initial point is uniquely determined by its initial velocity [5], and since we are given a value for the aircraft speed, we just need to determine the direction in which the aircraft is heading when it crosses each ping arc. To determine the heading direction we derive an equation that enforces the condition that the aircraft arrives at the next ping arc at the next ping time. We refer to this equation as the **ping arc equation**.

To study the ping arcs, we use a special **satellite coordinate system**, which is a rectangular coordinate system so that the origin is at the center of mass of the earth and the satellite is located on the positive x-axis (see Figure 2.1 (B)). Let $\{\mathbf{i}_S, \mathbf{j}_S, \mathbf{k}_S\}$ be the orthonormal basis for $\mathbf{R}^3$ whose elements are in the directions of the positive coordinate axes of such a coordinate system. We then define the **spherical satellite coordinates**, (Θ, Φ), of a unit vector, $\mathbf{y}$, by the equation

$$\mathbf{y} \;=\; \mathbf{y}(\Theta, \Phi) \;=\; \cos\Phi\,\mathbf{i}_S + \cos\Theta\sin\Phi\,\mathbf{j}_S + \sin\Theta\sin\Phi\,\mathbf{k}_S. \tag{2.1}$$

Since all points on the same circle of latitude in the satellite coordinate system are at the same distance from the satellite (see Figure 1.1), the ping arcs are circles of latitude, $\Phi = c$, on the sphere of radius R_A. The red circles in Figure 2.1 are ping arcs.

Using the satellite coordinate system, the ping arc equation can be derived using trigonometry. However, rather than using a triangle in the plane whose sides are segments of straight lines, we will use a triangle on the sphere of radius, R_A, whose sides are segments of circles. This spherical triangle is the triangle ABC depicted in

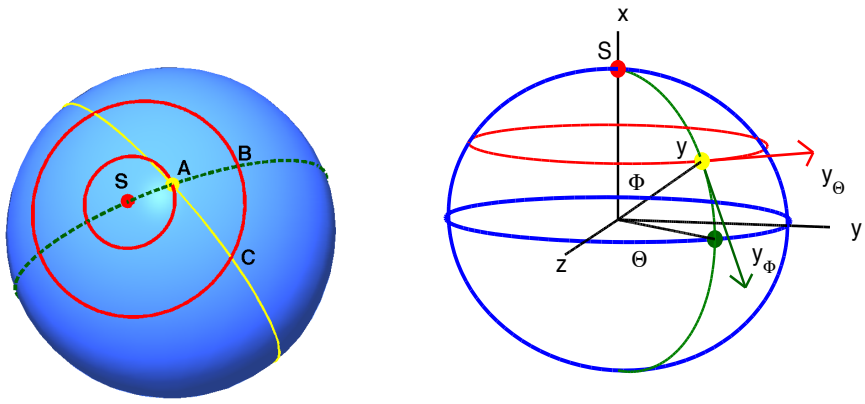

(A) (B)

FIG. 2.1 *(A) The spherical right triangle ABC used in the derivation of the ping arc equation. The red dot, S, is the projection of the satellite onto the blue sphere of radius, R_A. The two red curves are ping arcs, which are circles of latitude in the satellite coordinate system, and the dotted green curve is a circle of longitude. The flight path is the segment, AC, of the solid yellow great circle that forms the hypotenuse of the spherical right triangle. (B) The satellite coordinate system. The projection of the satellite onto the unit sphere is shown with a red dot. The unit vector, $\mathbf{y} = \mathbf{y}(\Theta, \Phi)$, in Equation 2.1 is shown with a yellow dot. The unit tangent vectors, $\mathbf{y}_\Theta$ and $\mathbf{y}_\Phi$, in Equation 2.4 are shown with red and green arrows, respectively.*

Figure 2.1 (A). The projection, S, of the satellite onto the sphere is shown with a red dot. The two solid red circles represent two ping arcs, which are circles of latitude in the satellite coordinate system. The dashed green curve is a circle of longitude in the satellite coordinate system that intersects the solid red circles of latitude at right angles. The initial position of the aircraft on the first ping arc is shown with a yellow dot. The flight path of the aircraft is the yellow great circle which forms the hypotenuse of the triangle. Since we know the distance, L, the aircraft travels between the two ping times, we just need to rotate the yellow great circle flight path about the initial position, A, until the length of the hypotenuse AC is L. Of course, if the distance, L, the aircraft travels is less than the geodesic distance, $|AB|$, between the two ping arcs, then the problem has no solution.

At the n-th ping time, t_n, the position, $\mathbf{r}_n$, of the aircraft can be expressed as

$$\mathbf{r}_n \;=\; R_A \mathbf{y}_n \;:=\; R_A \mathbf{y}(\Theta_n, \Phi_n), \tag{2.2}$$

where R_A is the radius of the sphere on which the aircraft is flying and (Θ_n, Φ_n) are the spherical satellite coordinates of the aircraft. For each $n \in \{1, 2, \cdots, N\}$, the **ping arc angle**, Φ_n, of the n-th ping arc can be calculated from the recorded BTO data, and by assumption Θ_1 is known. Our goal is to solve for $\Theta_2, \cdots, \Theta_N$ in succession. To that end, we observe that the great circle flight path, which at time, t_n, has position, $\mathbf{r}_n$, and velocity, $\mathbf{v}_n$, is parametrized by

$$\mathbf{r}_A(t) \;=\; \cos\left[\frac{v(t-t_n)}{R_A}\right] \mathbf{r}_n \;+\; \frac{R_A}{v} \sin\left[\frac{v(t-t_n)}{R_A}\right] \mathbf{v}_n, \tag{2.3}$$

where R_A is the radius of the sphere on which the great circle lies, and $v = |\mathbf{v}_n|$ is the known constant ground speed of the aircraft. Since the velocity vector, $\mathbf{v}_n$, is tangent

to the sphere at the point, $\mathbf{r}_n = R_A\mathbf{y}_n$, it can be expressed in the form

$$\mathbf{v}_n \;=\; v\cos\beta_n\,\mathbf{y}_{\Theta,n} \;+\; v\sin\beta_n\,\mathbf{y}_{\Phi,n}, \tag{2.4}$$

where the angle, β_n, is the unknown **heading direction** of the aircraft. Here $\mathbf{y}_{\Theta,n}$ and $\mathbf{y}_{\Phi,n}$ are unit vectors tangent to the coordinate curves, $\Phi = \Phi_n$ and $\Theta = \Theta_n$, respectively (see Figure 2.1 (B)).

The **ping arc equation**, which enforces the condition that the aircraft crosses the $(n+1)$-st ping arc at time t_{n+1} is therefore given by the vector equation

$$\mathbf{r}_A(t_{n+1}) \;=\; R_A\mathbf{y}(\Theta_{n+1},\Phi_{n+1}). \tag{2.5}$$

Since both sides are tangent to the sphere of radius, R_A, Equation (2.5) is really two independent equations in the two unknowns, β_n and Θ_{n+1}. As can be seen in Figure 2.1 (B), we can rotate the satellite coordinate system about the x-axis so that $\mathbf{r}_n$ is in the xy-plane (*i.e.*, $\Theta_n = 0$). Then, since the $\mathbf{i}_S$-component of $\mathbf{y}(\Theta_{n+1},\Phi_{n+1})$ is independent of Θ_{n+1} (see Equation (2.1)), we can eliminate Θ_{n+1} by taking the inner product of Equation (2.5) with the vector $\mathbf{i}_S$. Solving for the heading direction, β_n, we obtain

$$\sin\beta_n \;=\; \frac{\cos\left(\frac{v\Delta t_n}{R_A}\right)\cos\Phi_n \;-\; \cos\Phi_{n+1}}{\sin\left(\frac{v\Delta t_n}{R_A}\right)\sin\Phi_n}. \tag{2.6}$$

If $\beta_n \neq \pm\pi/2$ then there are two distinct solutions, $\beta_n^{\pm}$, of Equation (2.6), one with $\cos\beta_n^{+} > 0$ and the other with $\cos\beta_n^{-} < 0$.

In Figure 2.2 (A), we show three constant speed flight paths for MH370 that were computed using Model I. These flight paths are very similar to flight paths that were found by the Satellite Working Group and that were used between March 17th and April 1st to define a series of search areas for the missing aircraft [2].

2.1. Problems.

1. Provide geometric and algebraic justifications for Equation (2.3).$^{(*)}$
2. Make a sketch illustrating the geometric relationship between β_n and the circles of longitude and latitude in the spherical satellite coordinate system.
3. Fill in the details of the derivation of Equation (2.6).$^{(*)}$
4. For all ping times except the first, you can usually make a reasonable guess for which of the two solutions, $\beta_n^{\pm}$, of Equation (2.6) to choose. How? Why only usually? As a result, we can usually obtain two plausible flight paths, one with $\beta_1 = \beta_1^{+}$ and the other with $\beta_1 = \beta_1^{-}$. We will refer to these as the **positive and negative flight paths**.
5. Recall that our goal was to solve for Θ_{n+1}. How do you do that?
6. In Section 7, we will see that there is some uncertainty in the initial position, Θ_1, of MH370. With Model I, if you rotate the initial position, Θ_1, of the aircraft on the first ping arc by $\Delta\Theta_1$, what happens to final position, Θ_N? Discuss possible implications for the problem of determining search areas for MH370.
7. Write a computer program that implements Model I and validate it by comparison with ping arc data obtained from simulated flight paths.
8. Assuming that the position, $\mathbf{r}_n = R_A\mathbf{y}(\Theta_n,\Phi_n)$, of the aircraft on the n-th ping arc is known, numerically and/or analytically quantify the uncertainty

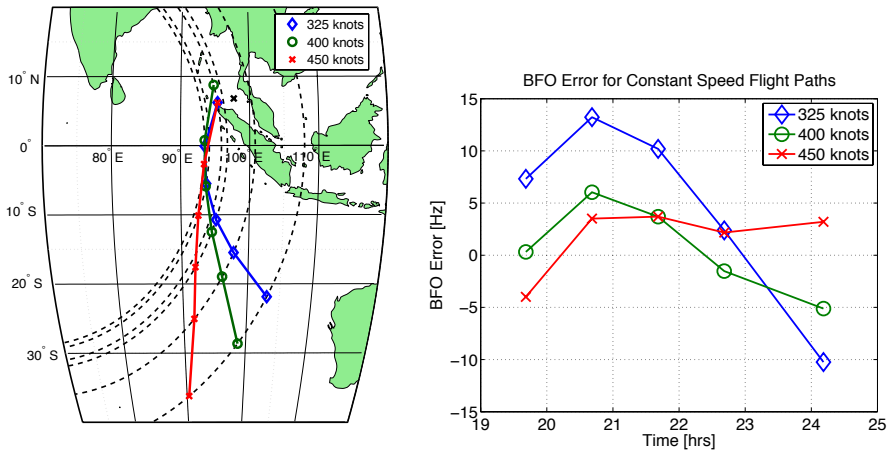

(A) (B)

FIG. 2.2 *(A) Three constant speed flight paths for MH370 computed using Model I. The ground speeds for these flight paths are 325 knots (602 km/hr), 400 knots (741 km/hr), and 450 knots (833 km/hr). The position of MH370 at last radar contact is shown with the black cross. (B) The differences between the BFO values of each of the three flight paths shown on the left and the recorded BFO values given in Table 1.1. The BFO errors at 18:28 UTC, which are not shown, are approximately* -50 *Hz.*

in the position, $\mathbf{r}_{n+1}$, of the aircraft at the next ping time, t_{n+1}, due to uncertainty in either (a) the speed, v, of the aircraft, (b) the altitude of the aircraft, or (c) the ping arc angle, Φ_{n+1}. To what degree do these uncertainties in $\mathbf{r}_{n+1}$ depend on the choice of Φ_n?

3. The Doppler shift and Burst Frequency Offset. As discussed in the Introduction, the Doppler shift is a frequency shift in an electromagnetic signal that is transmitted by one object (the aircraft) and received by another object (the satellite). The Doppler shift can be expressed in terms of the relative velocity vector, $\mathbf{v} = \mathbf{v}_A - \mathbf{v}_S$, and the unit displacement vector $\widehat{\mathbf{u}} = (\mathbf{r}_A - \mathbf{r}_S)/\|\mathbf{r}_A - \mathbf{r}_S\|$ of the aircraft with respect to the satellite. Specifically, the Doppler shift, Δf, is proportional to the component of $\mathbf{v}$ in the line of sight direction, $\widehat{\mathbf{u}}$:

$$\frac{\Delta f}{f} \;=\; -\frac{1}{c}\,\widehat{\mathbf{u}}\cdot\mathbf{v}. \tag{3.1}$$

Here f is the frequency of the transmitted signal and c is the speed of light.

We now derive a formula for the aircraft-satellite Doppler shift at each ping time under the assumption that the satellite is in a geostationary orbit. In Section 5, we will extend this formula to the more realistic case of a geosynchronous satellite orbit. In terms of the orthonormal basis, $\{\mathbf{i}_S, \mathbf{j}_S, \mathbf{k}_S\}$, associated with the satellite coordinate system discussed in Section 2, the position of the geostationary satellite is of the form $\mathbf{r}_S = R_S\mathbf{i}_S$, where R_S is the radius of the satellite orbit as measured from the center of mass of the earth. In addition, the position of the aircraft at the n-th ping time is given by $\mathbf{r}_A(t_n) = R_A\mathbf{y}(\Theta_n, \Phi_n)$, and the velocity of the aircraft is given by

$$\mathbf{v}_A(t_n) \;=\; \mathbf{v}_n \;=\; v_{\Theta,n}\mathbf{y}_{\Theta,n} \;+\; v_{\Phi,n}\mathbf{y}_{\Phi,n}. \tag{3.2}$$

Here $v_{\Theta,n}$ and $v_{\Phi,n}$ are the components of the aircraft velocity that are respectively parallel and perpendicular to the n-th ping arc.[2] Since $\widehat{\mathbf{u}}(t_n) \cdot \mathbf{y}_{\Theta,n} = 0$, we find that for a geostationary satellite, the aircraft-satellite Doppler shift, Δf_n, at the n-th ping arc is related to the component, $v_{\Phi,n}$, of the aircraft velocity that is perpendicular to the ping arc by

$$\Delta f_n \;=\; -\frac{f}{c}\frac{R_S}{D_{\mathrm{SA},n}}\, v_{\Phi,n} \sin\Phi_n, \tag{3.3}$$

where the distance between the satellite and aircraft is given by

$$D_{\mathrm{SA},n} \;=\; \sqrt{R_S^2 - 2R_S R_A \cos\Phi_n + R_A^2}. \tag{3.4}$$

The Inmarsat communications system is not able to directly record the aircraft-satellite Doppler shift. However, the values of a closely related quantity—the Burst Frequency Offset (BFO)—were logged by the satellite ground station in Perth. The BFO can be regarded as the difference between the frequency actually received by the ground-station and the frequency it is designed to receive. To optimize performance, satellite communications systems are designed to keep the BFO small. One of the main contributions to the BFO is the Doppler shift, Δf_{AS}, between the aircraft and the satellite, which is in a geosynchronous orbit, and is thus moving relative to the earth. To prevent the BFO from becoming too large, the aircraft uses knowledge of its current position to partially compensate for Δf_{AS} by shifting the frequency it transmits by the Doppler shift, $\Delta f_{\text{AS-Comp}}$, due to the relative motion of the aircraft and an imaginary geostationary satellite, located at an altitude of 35,786 km above the point on the equator at longitude 64.5°E. Overall, the BFO is given by [2]

$$\mathrm{BFO} \;=\; \Delta f_{\mathrm{AS}} - \Delta f_{\text{AS-Comp}} + \Delta f_{\mathrm{SG}} + \delta f_{\mathrm{AI}} + \delta f_{\mathrm{Bias}}, \tag{3.5}$$

where Δf_{SG} is the Doppler shift between the geosynchronous satellite and the ground station, δf_{AI} is a known time-dependent aircraft-independent frequency shift [2], and δf_{Bias} is a time-independent frequency shift.

In Figure 2.2 (B), we show the difference in the BFO between the model and the data in Table 1.1, for each of the flight paths in Figure 2.2 (A). For these results we used the nominal value of $\delta f_{\mathrm{Bias}} = 150$ Hz for the time-independent frequency shift. The reported uncertainty in δf_{Bias} is ± 5 Hz [2]. The small differences between the BFO values of these three reconstructed flight paths together with the large uncertainty in δf_{Bias} demonstrate the significant challenges the Satellite Working Group faced in narrowing the search area.

3.1. Problems.

1. Give a geometric explanation and an algebraic proof for why $\widehat{\mathbf{u}}(t_n) \cdot \mathbf{y}_{\Theta,n} = 0$, and hence derive Equation (3.3).$^{(*)}$
2. With a geostationary satellite model, it is impossible to use Doppler shift data to break the symmetry (*i.e.*, distinguish) between the positive and negative flight paths. Why?
3. Show that with a geostationary satellite model, it is impossible to use ping arc angle and Doppler shift data to distinguish between two flight paths that are rotations of each other about the satellite axis.

[2] For convenience from now on we choose to work with $v_{\Theta,n}$ and $v_{\Phi,n}$ rather than with the variables v_n and β_n in Equation (2.4).

4. A Model of the Satellite Motion. In Section 2, we determined the velocity, $\mathbf{v}_n$, by assuming knowledge of the speed, v, and using Equation (2.6) to solve for the heading, β_n. However, by now you may have realized that we could instead determine the velocity, $\mathbf{v}_n$, by using Equation (3.3) to solve for $v_{\Phi,n}$ in terms of the Doppler-shift data, Δf_n, and then reformulating Equation (2.5) to solve for $v_{\Theta,n}$. This observation forms the basis of Model II, described in Section 5 below. However, to break the symmetry between the positive and negative flight paths, in this section we replace the geostationary satellite model used in Section 2 with a more realistic geosynchronous satellite model to be used in Section 5. Specifically, we derive a formula for the position and velocity of the Inmarsat 3-F1 satellite in a coordinate system that rotates with the earth. We will develop this formula using publicly available data that gives the position and velocity of the satellite at 1 second intervals on the day that MH370 disappeared.[3] Although it may be more accurate to use this data directly, we include the satellite model presented in this section to provide the reader with a better understanding of the nature of the satellite orbit.

If we assume that the motion of the satellite is determined solely by the gravitational force exerted by the earth, then the satellite will move in a nearly-circular elliptical orbit whose center is at the center of mass of the earth. Ideally, the orbit of a communications satellite should be geostationary. Assuming that the orbit is a perfect circle in the equatorial plane, the radius of such an orbit is 42,157 kilometers, which is about 6.6 times the radius of the earth. However, it is not possible to achieve a perfect geostationary orbit due to the gravitational effects of the moon and sun, together with the flattening of the earth at the poles [9]. Instead, over time the orbital plane of the satellite tilts slightly with respect to the equatorial plane of the earth. Consequently, the satellite orbit is at best geosynchronous, *i.e.*, the satellite returns to the same point in the sky at the same time each day. In general, the projection onto the surface of the earth of the path of a geosynchronous satellite is a curve called an analemma, which depending on the values of the parameters of the orbit, can be a figure-eight or tear-drop shaped curve [11]. In particular, as we see in Figure 1.2 (B), the Inmarsat 3-F1 satellite traces out a curve on the earth that looks like a very narrow teardrop-shaped curve.

The motion of a satellite about the earth is most readily described using an Earth-Centered Inertial (ECI) coordinate system in which the origin is at the center of mass of the earth and with respect to which the earth and the satellite rotate [12]. However, the motion of an aircraft relative to a satellite is best described using a coordinate system that rotates with the earth. A standard choice for such a coordinate system is the Earth-Centered Earth-Fixed (ECEF) coordinate system [13] which places the origin at the center of mass of the earth and for which the z-axis is aligned with a reference north pole and the xz-plane is aligned with a reference prime meridian (i.e, a great circle with 0° longitude). For simplicity, we assume that the axis of rotation of the earth is aligned with the reference north pole, although this is not exactly the case. Any of the geostationary satellite coordinate systems in Section 2 can be obtained from the ECEF coordinate system by a rotation that maps the point on the equator at 0° longitude to the projection of the satellite onto the surface of the earth. A major goal of this section is to define a geosynchronous satellite coordinate system that is obtained from the ECEF coordinate system by a rotation that maps the north pole of the earth onto a normal vector to the orbital plane of the satellite (a slight tilt), and maps the point on the equator at 0° longitude to the projection of the

[3] A copy of this data was sent to the author and is included in the supplementary material.

satellite onto the surface of the earth (see Equation (4.13) below). Since the satellite moves with respect to a point on the earth, the geosynchronous satellite coordinate system changes with time.

Since we will make extensive use of vector algebra and since we need to convert between several different earth-centered rectangular coordinate systems we make use of the notion of the **frame** (i.e., the *ordered orthonormal basis*) that is canonically associated with a given positively oriented rectangular coordinate system. We begin by recalling the following results from Linear Algebra.

LEMMA 4.1. *Let $\mathcal{B} = \{\mathbf{v}_1, \mathbf{v}_2, \mathbf{v}_3\}$ be an ordered basis for $\mathbf{R}^3$ and let $\mathbf{u} \in \mathbf{R}^3$. Then*

$$\mathbf{u} = \sum_{j=1}^{3} \alpha_j \ \mathbf{v}_j \iff \mathbf{u} \ = \ \begin{bmatrix} \mathbf{v}_1 & \mathbf{v}_2 & \mathbf{v}_3 \end{bmatrix} \begin{bmatrix} \alpha_1 \\ \alpha_2 \\ \alpha_3 \end{bmatrix}. \tag{4.1}$$

Furthermore, if $\mathbf{B}$ is an orthonormal basis then $\alpha_j = \mathbf{u} \cdot \mathbf{v}_j$.

PROPOSITION 4.2. *Let $\mathcal{B} = \{\mathbf{v}_1, \mathbf{v}_2, \mathbf{v}_3\}$ and $\mathcal{C} = \{\mathbf{w}_1, \mathbf{w}_2, \mathbf{w}_3\}$ be two frames for $\mathbf{R}^3$. Then there is an orthogonal matrix, $\mathbf{R}$, so that*

$$\begin{bmatrix} \mathbf{w}_1 & \mathbf{w}_2 & \mathbf{w}_3 \end{bmatrix} \ = \ \begin{bmatrix} \mathbf{v}_1 & \mathbf{v}_2 & \mathbf{v}_3 \end{bmatrix} \mathbf{R}. \tag{4.2}$$

Geometrically, the matrix $\mathbf{R}$ rotates the frame $\mathcal{B}$ onto the frame $\mathcal{C}$.

In particular, we will use the orthogonal matrix

$$\mathbf{R}(\theta, \phi) \ = \ \begin{bmatrix} \cos\theta\cos\phi & -\sin\theta & \cos\theta\sin\phi \\ \sin\theta\cos\phi & \cos\theta & \sin\theta\sin\phi \\ -\sin\phi & 0 & \cos\phi \end{bmatrix}, \tag{4.3}$$

which has the properties that $\mathbf{R}(\theta) := \mathbf{R}(\theta, 0)$ is rotation through an angle θ about the z-axis, and

$$\mathbf{R}(\theta_1)\,\mathbf{R}(\theta_2, \phi) \ = \ \mathbf{R}(\theta_1 + \theta_2, \phi). \tag{4.4}$$

Let $\mathcal{E} = \{\mathbf{i}_E, \mathbf{j}_E, \mathbf{k}_E\}$ be the frame associated with the ECEF coordinate system and let $\mathcal{F} = \{\mathbf{i}_F, \mathbf{j}_F, \mathbf{k}_F\}$ be the frame associated with the non-rotating ECI coordinate system. The rotation of the earth about its axis is then modeled by applying Proposition 4.2 to express the ECEF frame in terms of the ECI frame. Since our goal is to obtain a formula for the motion of the satellite with respect to the earth, we instead express the ECI frame in terms of the ECEF frame via the matrix equation

$$\begin{bmatrix} \mathbf{i}_F & \mathbf{j}_F & \mathbf{k}_F \end{bmatrix} \ = \ \begin{bmatrix} \mathbf{i}_E & \mathbf{j}_E & \mathbf{k}_E \end{bmatrix} \mathbf{R}(-\alpha t). \tag{4.5}$$

Here t denotes time and $\alpha = 2\pi/T$, where $T = 23.934$ hrs is the period of rotation of the earth about its axis [8].

An analysis of the satellite position and velocity data shows that the orbital plane of the satellite is a slight tilt (a rotation) of the equatorial plane of the earth, and that in this plane the satellite orbit is a small perturbation of a constant speed circle. Specifically, we can choose a frame $\mathcal{P} = \{\mathbf{i}_P, \mathbf{j}_P, \mathbf{k}_P\}$ for which the vector, $\mathbf{k}_P$, is the normal vector to the orbital plane of the satellite, and which is a rotation of the ECI frame, $\mathcal{F}$, of the form

$$\begin{bmatrix} \mathbf{i}_P & \mathbf{j}_P & \mathbf{k}_P \end{bmatrix} \ = \ \begin{bmatrix} \mathbf{i}_F & \mathbf{j}_F & \mathbf{k}_F \end{bmatrix} \mathbf{R}(\theta_P, \phi_P) \ = \ \begin{bmatrix} \mathbf{i}_E & \mathbf{j}_E & \mathbf{k}_E \end{bmatrix} \mathbf{R}(\theta_P - \alpha t, \phi_P), \tag{4.6}$$

where the second equality follows from Equations (4.5) and (4.4). Since we will perform all numerical computations in the ECEF frame, we may assume that $\begin{bmatrix}\mathbf{i}_E & \mathbf{j}_E & \mathbf{k}_E\end{bmatrix}$ is the identity matrix.

Furthermore, using the satellite data we found that the distance, $R_S(t)$, of the satellite from the center of mass of the earth and the speed, $v_S(t)$, of the satellite are well approximated by functions of the form

$$R_S(t) = \overline{R}_S[1+\epsilon_S \sin(\alpha(t-t_0))], \tag{4.7}$$
$$v_S(t) = \overline{v}_S[1-\epsilon_S \sin(\alpha(t-t_0))], \tag{4.8}$$

where the mean radius is $\overline{R}_S = 4.216\times 10^4$ km, the mean speed is $\overline{v}_S = \alpha\overline{R}_S = 1.107\times 10^4$ km/hr, the offset time is $t_0 = 13.608$ hrs (UTC), and the perturbation parameter is $\epsilon_S = 5.298\times 10^{-4}$. In addition, the satellite crosses the equatorial plane of the earth at the times $t\in\{t_0, t_0+T/2\}$ for which $R_S(t)=\overline{R}_S$. Consequently, the satellite trajectory is well approximated by the parametrized curve

$$\mathbf{r}_S(t) = R_S(t)\left[\cos\theta_S(t)\,\mathbf{i}_P + \sin\theta_S(t)\,\mathbf{j}_P\right], \tag{4.9}$$

where

$$\theta_S(t) = \frac{\pi}{2} + \int_{t_0}^{t}\frac{v_S(s)}{R_S(s)}\,ds \approx \theta_0 + \alpha t + 2\epsilon_S C(t) + \mathcal{O}(\epsilon_S^2), \tag{4.10}$$

where $\theta_0 = \frac{\pi}{2} - \alpha t_0$ and $C(t) = \cos[\alpha(t-t_0)] - 1$. By construction, this curve has radial and speed functions given by $\|\mathbf{r}_S(t)\| = R_S(t)$ and $\|\mathbf{r}_S'(t)\| = v_S(t) + \mathcal{O}(\epsilon_S^2)$, respectively. Moreover, the curve lies in the plane through the origin with normal $\mathbf{k}_P$, and crosses the equator at time t_0 with $\mathbf{r}_S(t_0) = \overline{R}_S\mathbf{j}_P = \overline{R}_S[-\sin\theta_P\mathbf{i}_F + \cos\theta_P\mathbf{j}_F]$. Using the satellite position data, we estimated the vectors $\mathbf{j}_P$ and $\mathbf{k}_P$ and hence deduced that $(\theta_P,\phi_P) = (179.25^\circ, 1.64^\circ)$.

By Lemma 4.1 and Equations (4.9), (4.3) and (4.6),

$$\mathbf{r}_S(t) = R_S(t)\begin{bmatrix}\mathbf{i}_P & \mathbf{j}_P & \mathbf{k}_P\end{bmatrix}[\mathbf{R}(\theta_S(t))]_{*1} = R_S(t)\,\mathbf{R}(\theta_P-\alpha t,\phi_P)\,[\mathbf{R}(\theta_S(t))]_{*1}, \tag{4.11}$$

where $\mathbf{A}_{*j}$ denotes the j-th column of the matrix $\mathbf{A}$. A calculation then shows that

$$\mathbf{r}_S(t) = R_S(t)\begin{bmatrix}-\delta_C\cos[\theta_S(t)+\alpha t-\theta_P] + (1-\delta_C)\cos[\theta_S(t)-\alpha t+\theta_P]\\ \delta_C\sin[\theta_S(t)+\alpha t-\theta_P] + (1-\delta_C)\sin[\theta_S(t)-\alpha t+\theta_P]\\ -\delta_S\cos\theta_S(t)\end{bmatrix}, \tag{4.12}$$

where $\delta_C = \frac{1}{2}(1-\cos\phi_P)$ and $\delta_S = \sin\phi_P$ are both close to zero. In Figure 1.2 (B), we show the projection of the satellite orbit onto the surface of the earth. Notice that the longitudinal scale is much smaller than the latitude scale. The position error between the data (blue) and model (red) is less than 6 km and the velocity error is less than 0.5 km/hr (as measured in the ECI coordinate system).

In analogy with the geostationary satellite coordinate system in Section 2, we introduce a time-dependent geosynchronous satellite coordinate system via the **moving satellite frame**, $\mathcal{S}(t)$, defined in terms of the ECEF frame, $\mathcal{E}$, by

$$\begin{bmatrix}\mathbf{i}_S(t) & \mathbf{j}_S(t) & \mathbf{k}_S(t)\end{bmatrix} = \begin{bmatrix}\mathbf{i}_E & \mathbf{j}_E & \mathbf{k}_E\end{bmatrix}\mathbf{R}(\theta_P-\alpha t,\phi_P)\,\mathbf{R}(\theta_S(t)). \tag{4.13}$$

Comparing the first column of Equation (4.13) to Equation (4.11), we have that

$$\mathbf{r}_S(t) = R_s(t)\,\mathbf{i}_S(t). \tag{4.14}$$

Explicit formula for $\mathbf{j}_S$ and $\mathbf{k}_S$ can be obtained from Equation (4.12) by observing that $\mathbf{j}_S = \frac{d}{d\theta_S}\mathbf{i}_S$ and $\mathbf{k}_S = \mathbf{i}_s\times\mathbf{j}_S$.

4.1. Problems.

1. Show that when $\epsilon_S = 0$ in Equation (4.10), $\mathbf{r}_S$ is a figure-eight curve that lies on the intersection of a sphere and a cylinder. Also, find an analytical relationship between the tilt angle, ϕ_P, and the amplitude of the oscillations in the latitude and longitude of $\mathbf{r}_S$.
2. Devise a method to estimate $\mathbf{k}_P$ from the satellite position data.
3. Prove the approximate formula for θ_S in Equation (4.10) and show that the curve, $\mathbf{r}_S$, defined by Equation (4.9) has the properties given below (4.10).$^{(*)}$
4. Verify Equation (4.12) and derive an explicit formula for $\mathbf{j}_S$.$^{(*)}$
5. The concept of a moving frame, due to E. Cartan, plays an important role in differential geometry. Cartan's basic idea is to assign a frame to each point of an object being studied (e.g., a curve or surface), and then use the orthonormal expansion in Lemma 4.1 to express the rate of change of the frame in terms of the frame itself [5]. Use this idea to find an explicit formula for the satellite velocity in terms of the moving satellite frame.
6. Write a computer program to reproduce Figure 1.2 (B).
7. Make animations of the satellite orbit viewed in both the ECI and ECEF coordinate systems.

5. Model II: The Unknown-Speed, Concatenation-of-Geodesics Model.

In this section, we describe a model in which the flight path of the aircraft is approximated by a concatenation of segments of constant-speed great circles (geodesics) on the sphere, but for which the different segments can have different *a priori* unknown speeds. We employ the geosynchronous satellite motion model developed in Section 4 and make use of Doppler shift data at the ping times. As in Model I, the initial position of the aircraft is an input parameter to the model. The equations in the model are generalizations to the case of a geosynchronous satellite of the ping arc equation (2.5) and the Doppler shift equation (3.3). Given knowledge of the aircraft position, $\mathbf{r}_n$, on the current ping arc, our goal is to derive a system of three equations in which the unknowns are the two components, $v_{\Theta,n}$ and $v_{\Phi,n}$, of the aircraft velocity at the current ping time and the position, Θ_{n+1}, of the aircraft on the next ping arc. These three equations are a vector ping arc equation (two scalar equations), which enforces the condition that the aircraft reaches the next ping arc at the next ping time, and a Doppler shift equation which enforces the condition that the aircraft departs from the current ping arc with the correct Doppler shift. However, in practice we found that a more robust approach is to solve the overdetermined system consisting of these three equations together with a second Doppler shift equation, which enforces the condition that the aircraft arrives at the next ping arc with the correct Doppler shift.

To perform the calculations, we make use of two moving frames. These are the **moving satellite frame**, $\{\mathbf{i}_{\mathrm{S},n}, \mathbf{j}_{\mathrm{S},n}, \mathbf{k}_{\mathrm{S},n}\}$, given by evaluating Equation (4.13) at the n-th ping time, t_n, and the **moving aircraft frame**, $\{\mathbf{y}_n, \mathbf{y}_{\Phi,n}, \mathbf{y}_{\Theta,n}\}$, which is chosen so that at time t_n the aircraft position and velocity are of the form $\mathbf{r}_n = R_A\mathbf{y}(\Theta_n, \Phi_n) =: R_A\mathbf{y}_n$ and $\mathbf{v}_n = v_{\Theta,n}\mathbf{y}_{\Theta,n} + v_{\Phi,n}\mathbf{y}_{\Phi,n}$, as in Equations (2.2) and (3.2). If we let $\mathbf{F}_n$ be the 3×3 orthogonal matrix

$$\mathbf{F}_n = \begin{bmatrix} \mathbf{i}_{\mathrm{S},n} & \mathbf{j}_{\mathrm{S},n} & \mathbf{k}_{\mathrm{S},n} \end{bmatrix}, \tag{5.1}$$

then, by Lemma 4.1,

$$\begin{bmatrix}\mathbf{y}_n & \mathbf{y}_{\Phi,n} & \mathbf{y}_{\Theta,n}\end{bmatrix} \;=\; \mathbf{F}_n \begin{bmatrix} \cos\Phi_n & -\sin\Phi_n & 0 \\ \cos\Theta_n \sin\Phi_n & \cos\Theta_n\cos\Phi_n & -\sin\Theta_n \\ \sin\Theta_n\sin\Phi_n & \sin\Theta_n\cos\Phi_n & \cos\Theta_n \end{bmatrix} =: \; \mathbf{F}_n\mathbf{Y}_n, \tag{5.2}$$

where the ping arc angles, Φ_n, can be obtained from the BTO data.

Using Equations (4.14), (5.2), and (3.2), we can express the vectors $\widehat{\mathbf{u}}$ and $\mathbf{v}$ in the Doppler shift formula (3.1) in terms of the moving satellite frame, to obtain the **first Doppler shift equation**, which expresses the difference between measured Doppler shift data, Δf_n, at the n-th ping time and an analytical formula for the Doppler shift in terms of parameters describing the motion of the aircraft and satellite, as

$$\begin{aligned} f_{\text{Doppler},1}(v_{\Phi,n}) \;:=\; \Delta f_n \;-\; \frac{f}{cD_{\text{SA},n}}\,[-v_{\Phi,n}R_{S,n}\sin\Phi_n - (R_{S,n} - R_A\cos\Phi_n)(\mathbf{v}_{S,n})_1 \\ +\; R_A\cos\Theta_n\sin\Phi_n(\mathbf{v}_{S,n})_2 + R_A\sin\Theta_n\sin\Phi_n(\mathbf{v}_{S,n})_3] \;=\; 0. \end{aligned} \tag{5.3}$$

Here $R_{S,n} = \|\mathbf{r}_S(t_n)\|$ is the distance of the satellite from the center of the earth, and by Lemma (4.1), $\mathbf{v}_{S,n} = \mathbf{F}_n^T\mathbf{r}_S'(t_n)$ is the coordinate vector of the satellite velocity in the moving satellite frame. Note that we can analytically solve Equation (5.3) for $v_{\Phi,n}$ in terms of known quantities. More importantly, due to the motion of the geosynchronous satellite in the ECEF frame (*i.e.*, as $\mathbf{v}_{S,n} \neq 0$), we see that Δf_n depends on Θ_n. Therefore, the symmetry we observed between the positive and negative flight paths with the geostationary satellite in Model I is broken.

Next, we derive the ping arc equations. By Equation (5.2), we have that at time t_n the position and velocity of the aircraft are given by $\mathbf{r}_n = R_A\mathbf{F}_n(\mathbf{Y}_n)_{*1}$ and

$$\mathbf{v}_n \;=\; \mathbf{F}_n\begin{bmatrix}(\mathbf{Y}_n)_{*2} & (\mathbf{Y}_n)_{*3}\end{bmatrix}\begin{bmatrix}v_{\Phi,n}\\ v_{\Theta,n}\end{bmatrix}. \tag{5.4}$$

Substituting these expressions into the Equation (2.3) for the great circle path we find that the position of the aircraft at time t_{n+1} is given by

$$\mathbf{r}_{n+1} \;=\; R_A\mathbf{F}_n\mathbf{Y}_n\mathbf{x}_n, \tag{5.5}$$

where $\mathbf{x}_n = \mathbf{x}_n(v_{\Phi,n}, v_{\Theta,n})$ is the unit column vector defined by

$$\mathbf{x}_n \;=\; \frac{1}{v_n}\begin{bmatrix}v_n\cos(v_n\Delta t_n/R_A) & v_{\Phi,n}\sin(v_n\Delta t_n/R_A) & v_{\Theta,n}\sin(v_n\Delta t_n/R_A)\end{bmatrix}^T. \tag{5.6}$$

Here $v_n = \sqrt{v_{\Phi,n}^2 + v_{\Theta,n}^2}$ is the aircraft speed at time t_n and $\Delta t_n = t_{n+1} - t_n$. On the other hand, the condition that the aircraft cross the $(n+1)$-st ping arc at time t_{n+1} can be expressed as $\mathbf{r}_{n+1} = R_A\mathbf{F}_{n+1}\mathbf{y}_{n+1}$, which together with Equation (5.5) yields the **vector ping arc equation**

$$\mathbf{x}_n(v_{\Phi,n}, v_{\Theta,n}) \;=\; \mathbf{A}_n y_{n+1}(\Theta_{n+1}, \Phi_{n+1}) \qquad \text{where } \mathbf{A}_n = \mathbf{Y}_n^T\mathbf{F}_n^T\mathbf{F}_{n+1} \text{ is orthogonal.} \tag{5.7}$$

Equation (5.7) is two independent equations in the three unknowns, $v_{\Phi,n}$, $v_{\Theta,n}$, and Θ_{n+1}. Just as in the derivation of Equation (2.6) for the aircraft heading, we can eliminate Θ_{n+1} to obtain the **scalar ping arc equation**

$$f_{\text{Ping}}(v_{\Phi,n}, v_{\Theta,n}) \;:=\; R_A\{(\mathbf{x}_n)_1 - a - \mathbf{b}^T\mathbf{x}_n\} \;=\; 0, \tag{5.8}$$

where $a = (\mathbf{A}_n)_{11} \cos \Phi_{n+1}$ and $\mathbf{b}^T = (\mathbf{A}_n)_{12}(\mathbf{A}_n^T)_{2*} + (\mathbf{A}_n)_{13}(\mathbf{A}_n^T)_{3*}$ are known.

Finally, we leave it as an exercise to the reader to formulate the **second Doppler shift equation** which is of the form[4]

$$f_{\text{Doppler},2}(v_{\Phi,n}, v_{\Theta,n}) \;=\; \Delta f_{n+1} \;-\; g(v_{\Phi,n}, v_{\Theta,n}) \;=\; 0. \tag{5.9}$$

The simplest method to solve for Θ_{n+1} is to use the first Doppler shift equation (5.3) to solve for $v_{\Phi,n}$, whereupon the scalar ping arc equation (5.8) can be used to solve for $v_{\Theta,n}$. Then Equation (5.7) can be inverted to obtain Θ_{n+1} from $\mathbf{y}_{n+1}$. While this method works well when the flight path is a great circle and the data is exact, it can fail for more general flight paths or for uncertain data. In that case, a more robust method is to minimize the function

$$F(v_{\Phi,n}, v_{\Theta,n}) = f^2_{\text{Doppler},1}(v_{\Phi,n}) + f^2_{\text{Ping}}(v_{\Phi,n}, v_{\Theta,n}) + f^2_{\text{Doppler},2}(v_{\Phi,n}, v_{\Theta,n}), \tag{5.10}$$

using unconstrained, gradient-based optimization (specifically, MATLAB's fminunc), and then solve for Θ_{n+1} using Equation (5.7). With a geostationary satellite, the analysis in Section 2 suggests that F has two local minima, corresponding to the positive and negative flight paths that go from the current ping arc to the next. With a geosynchronous satellite, numerical results strongly suggest that there is only a single local minimum, *i.e.*, that the symmetry between the positive and negative flight paths is indeed broken.

5.1. Problems.

1. Derive Equations (5.5) and (5.8).$^{(*)}$
2. Formulate Equation (5.9).$^{(*)}$
3. Given a value for $v_{\Phi,n}$ from Equation (5.3), use a Taylor series approximation and numerical simulations to show that Equation (5.8) is well approximated by a quadratic equation. Discuss the geometric significance of the roots of this quadratic.
4. Write a computer program that implements Model II and validate it by comparison with ping arc data obtained from simulated flight paths.
5. Using simulated flight paths, numerically investigate the uncertainty in the reconstructed flight path due to uncertainties in the Doppler shift data, Δf_n.

6. Model III: The Concatenation of Small Circles, BFO Model. In this section, we develop a fully numerical model in which the flight path of the aircraft is approximated by a concatenation of segments of small circles, and we use the BFO data that was recorded by the satellite ground station rather than the aircraft-satellite Doppler shift we used in Section 5.

A **small circle** on a sphere is the curve of intersection of the sphere with a plane. Great circles and circles of latitude are examples of small circles. The red curves in Figure 2.1 are small circles. Given an initial position on a sphere of radius, R_A, an initial velocity vector that is tangent to the sphere at the initial position, and a radius, R_C, that is less than the radius of the sphere, there are two small circle paths with the given initial position, initial velocity, and radius. From the point of view of an aircraft pilot, one small circle flight path turns to the right and the other to the left. Rather than parametrizing small circles in terms of their radius, R_C, it is more convenient to parametrize them in terms of their geodesic curvature, κ_g. The geodesic curvature of a constant speed smooth curve on a surface quantifies how much the curve is turning

[4] A formula for g is given in the Appendix in the supplementary material.

in the surface [5]. Since it does not turn in the surface, the geodesic curvature of a geodesic curve is zero. The geodesic curvature of a small circle path with constant speed, v, and radius, R_C, on a sphere of radius, R_A, is given by

$$\kappa_g = \pm v \sqrt{\frac{1}{R_C^2} - \frac{1}{R_A^2}}, \tag{6.1}$$

where the choice of sign depends on whether the small circle path is turning right or left. The geodesic curvature of a great circle is zero and, for small circles, $|\kappa_g| \to \infty$ as $R_C \to 0$.

A basic assumption in the models developed by the Satellite Working Group is that—after a certain time (19:41 UTC)—MH370 was operating without human control [1]. One possible scenario is that the aircraft was flying at constant speed and at a constant heading relative to the air. However, because of the effects of wind, the path of the aircraft over the earth may not have exactly been a great circle. Therefore a model based on small circles may produce a better approximation to the flight path than one based on great circles.

We now derive a parametrization of the small circle with geodesic curvature, κ_g, that lies on the sphere of radius, R_A, and which at time, t_n has position, $\mathbf{r}_n$, and velocity, $\mathbf{v}_n$. If we let $\mathbf{c}$ be the center and R_C be the radius of this small circle, then

$$\mathbf{r}(t) \;=\; \mathbf{c} \;+\; \cos\left[\frac{v(t-t_n)}{R_C}\right]\mathbf{r}_n^{\perp} \;+\; \frac{R_C}{v}\sin\left[\frac{v(t-t_n)}{R_C}\right]\mathbf{v}_n, \tag{6.2}$$

where $\mathbf{r}_n^{\perp} = \mathbf{r}_n - \mathbf{c}$ and $v = |\mathbf{v}_n|$. Let $\mathbf{w}_n = \frac{\mathbf{r}_n}{R_A} \times \frac{\mathbf{v}_n}{v}$, so that $\{\frac{\mathbf{r}_n}{R_A}, \frac{\mathbf{v}_n}{v}, \mathbf{w}_n\}$ is frame adapted to the small circle. Then a calculation shows that

$$\frac{\mathbf{r}(t)}{R_A} \;=\; \left[1 + \frac{\cos\alpha_n(t) - 1}{1+K^2}\right]\frac{\mathbf{r}_n}{R_A} \;+\; \frac{K(\cos\alpha_n(t)-1)}{1+K^2}\,\mathbf{w}_n \;+\; \frac{\sin\alpha_n(t)}{\sqrt{1+K^2}}\,\frac{\mathbf{v}_n}{v}, \tag{6.3}$$

where $K = R_A\kappa_g/v$ and $\alpha_n(t) = v(t-t_n)/R_C$.

One motivation for using small circles is that the ping arc equation and the two Doppler shift equations in the great circle model in Section 5 form an overdetermined system of three equations in two unknowns, $(v_{\Phi,n}, v_{\Theta,n})$. By adding the geodesic curvature, $\kappa_{g,n}$, as a third unknown, we can use the ping arc and BFO data to obtain a system of three equations in three unknowns of the form

$$f_{\mathrm{BFO},1}(v_{\Phi,n}, v_{\Theta,n}) \;=\; 0, \tag{6.4}$$

$$f_{\mathrm{Ping}}(v_{\Phi,n}, v_{\Theta,n}, \kappa_{g,n}) \;=\; 0, \tag{6.5}$$

$$f_{\mathrm{BFO},2}(v_{\Phi,n}, v_{\Theta,n}, \kappa_{g,n}) \;=\; 0. \tag{6.6}$$

Although we can derive BFO equations for small circle flight paths that are similar to the first and second Doppler shift equations (5.3) and (5.9), because of the need to transform between the geostationary and geosynchronous satellite coordinate systems, there is no longer any advantage to using an analytical approach such as that described in Section 5.

Instead, given a position, $\mathbf{r}_n$, on the n-th ping arc and a triple $(v_{\Phi,n}, v_{\Theta.n}, \kappa_{g,n})$, we define $f_{\mathrm{Ping}}(v_{\Phi,n}, v_{\Theta.n}, \kappa_{g,n})$ to be the geodesic distance on the sphere of radius, R_A, between $\mathbf{r}(t_{n+1})$ and the $(n+1)$-st ping arc, where $\mathbf{r}(t_{n+1})$ is computed using the small circle parametrization (6.3). Similarly, we can use the definition (3.5)

of the BFO to evaluate $f_{\text{BFO},1}$ at $(v_{\Phi,n}, v_{\Theta,n})$ by computing the Doppler shifts, $\Delta f_{\text{AS},n}$ and $\Delta f_{\text{AS-Comp},n}$ directly using the definition (3.1). Finally, we can evaluate $f_{\text{BFO},2}$ at $(v_{\Phi,n}, v_{\Theta.n}, \kappa_{g,n})$ using Equation (3.1), provided we first use the small circle parametrization (6.3) to calculate the position and velocity vectors of the aircraft at the next ping arc.

Since it is unlikely that the flight path of MH370 was really a concatenation of segments of small circles and since there is measurement error in the BTO and BFO data and additional uncertainty in some of the model parameters, we do not expect Equations (6.4), (6.5), and (6.6) to have an exact solution. For these reasons, we formulated the problem of solving the equations as a nonlinear least squares problem of the form: Find the set of parameters $(v_{\Phi,n}, v_{\Theta,n}, \kappa_{g,n})$ that minimizes the objective function

$$F \;=\; f_{\text{Ping}}^2 + f_{\text{BFO},1}^2 + f_{\text{BFO},2}^2 + f_{\text{Penalty}}^2, \tag{6.7}$$

where the function $f_{\text{Penalty}}(\kappa_g) = (\kappa_g/\kappa_{g,\text{Threshold}})^4$ is defined so as to penalize small circles that have a small radius and large speed. Without this penalty term the numerical solver can get stuck in physically unrealistic local minima. A numerical simulation study suggests that for the simulated flight paths we considered and for the recorded MH370 data, the function F has a unique global minimum, *i.e.*, its graph is bowl-shaped. If true, this observation is due to the fact that the satellite orbit is geosynchronous, and to the inclusion of the penalty term in Equation (6.7).

6.1. Problems.

1. Fill in the details of the derivation of Equation (6.3).$^{(*)}$
2. Provide a reasonable formula for the parameter $\kappa_{g,\text{Threshold}}$ in the penalty function, f_{Penalty}.
3. Discuss the relative merits of analytical versus fully numerical methods, both in the context of this article and more generally in engineering applications.
4. How are the methods developed in this article analogous to numerical methods for solving systems of ordinary differential equations?
5. Implement a fully numerical small circle model that uses Doppler shift rather than BFO data and study its performance.
6. Using a geosynchronous satellite model, try to construct two flight paths that have the same ping arc and Doppler shift data, but which are very far apart when they cross the final ping arc.

7. Results. We verified Models II and III using several simulated flights, two of which are shown in Figure 7.1. Both of these flight paths are small circles that start at 95.6°E, 6.8°N (near the point of last radar contact of MH370) and have a constant speed of 600 km/h (325 knots). The radius of the small circle path is 80% of the radius of the earth in Figure 7.1 (A) and 35% of the radius of the earth in Figure 7.1 (B). The ping times were chosen to be the same as for MH370. The ping arcs for the two flights are shown with black dashed curves. In Figure 7.1 (A) the aircraft travels northwest almost tangent to the ping arcs. In Figure 7.1 (B) the aircraft travels south and then southeast along a path that is similar to the 325 knot flight path for MH370 shown in Figure 2.2. The positions at which the simulated flight path crosses the ping arcs are shown with blue diamonds. The green circles and red crosses show the corresponding aircraft positions computed using Models II and III, respectively. The agreement obtained between the results using the models and the simulated flight paths is excellent, although with Model II (based on great circles) the agreement is not quite as good as with Model III (based on small circles).

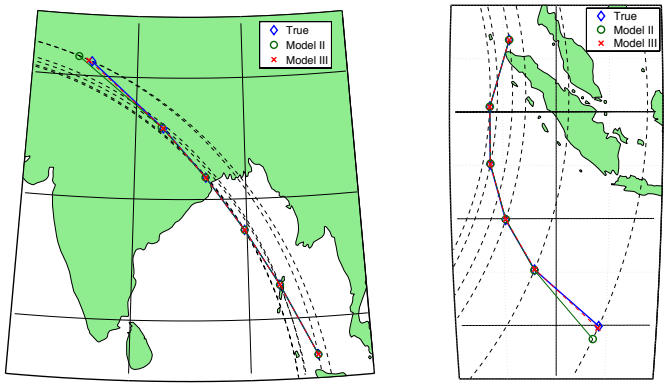

(A) (B)

FIG. 7.1 *Flight paths computed using Model II (green circles) and Model III (red crosses) for two simulated constant speed, small circle flight paths (blue diamonds). (A) The aircraft starts in the southeast corner of the map and travels northwest. (B) The aircraft starts in the northwest corner of the map and travels south and east.*

Next, we apply Model III to reconstruct the flight path of MH370, which requires addressing two major sources of uncertainty in the satellite data. First, because of large fluctuations in the BFO data recorded between 18:25 and 18:28, the flight path from 18:28 to 19:41 may not be well approximated by a segment of a small circle.[5] Following an approach taken in the ATSB report [2], we start the computation on the 19:41 ping arc using a range of initial positions, $\Theta_{19:41}$, that could reasonably be reached from the point of last radar contact at 18:15. In Figure 7.2 (A), we show this set of initial positions with a thin blue solid curve. The second source of uncertainty is the value of δf_{Bias} in Equation (3.5), which we varied from 145 Hz to 155 Hz to match the reported uncertainty [2]. For each pair $(\Theta_{19:41}, \delta f_{\text{Bias}})$, we used Model III to find the flight path that minimizes the objective function in Equation (6.7). To match the reported uncertainty in the BTO [2], we discarded flight paths for which there were ping times at which the distance of the aircraft from the ping arc exceeded 5 km. To quantify how well the computed flight paths fit the BFO data we calculated the **BFO goodness of fit**,

$$\text{GF}_{\text{BFO}} = \left[\sum_{k=1}^{K-1} |f^{(k)}_{\text{BFO},1}|^2\right]^{1/2} + \left[\sum_{k=2}^{K} |f^{(k)}_{\text{BFO},2}|\right]^{1/2}, \tag{7.1}$$

where k indexes the ping times from 19:41 to 24:11.

In Figure 7.2 (B), we show the BFO goodness of fit as a function of the longitude of the position of the aircraft on the 24:11 ping arc. Each blue circle corresponds to a different choice of the parameters $(\Theta_{19:41}, \delta f_{\text{Bias}})$. The minimum value of GF_{BFO} is 2.46 Hz at $(\Theta_{19:41}, \delta f_{\text{Bias}}) = (9.5°, 155)$. In Figure 7.2 (A), we show the corresponding flight path with the green circles. This flight path crosses the 24:11 ping arc at longitude 98.35°E. The ground speed of the aircraft varies from 917 km/hr to 800 km/hr which compares well with the typical air speed of 905 km/hr for a Boeing 777 at an

[5] This BFO data is not included in Table 1.1.

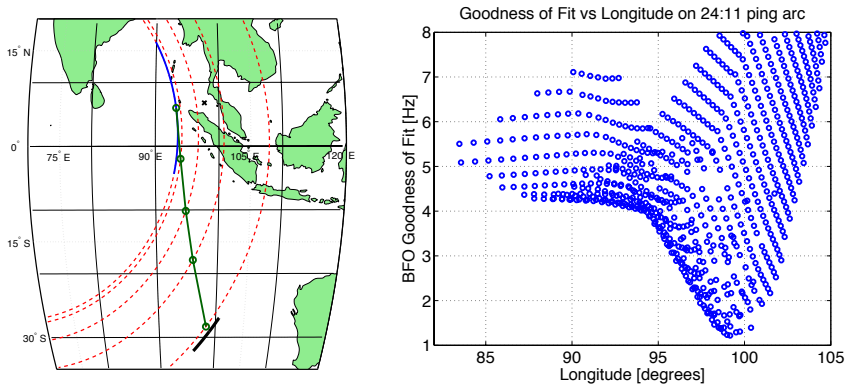

(A) (B)

FIG. 7.2 *(A) The flight path for MH370 computed using Model III with the values of* $(\Theta_{19:41}, \delta f_{Bias})$ *that minimize the BFO goodness of fit. The black cross shows the location of MH370 at last radar contact and the red dashed curves are the ping arcs from 19:41 to 24:11. The thin blue solid curve shows the set of initial positions,* $\Theta_{19:41}$*, on the 19:41 ping arc. The thick black curve shows the priority search area determined by the ATSB [2]. (B) Each blue circle shows the BFO goodness of fit of a flight path as a function of the longitude of the aircraft when it crosses the 24:11 ping arc. The different blue circles correspond to different values for* $(\Theta_{19:41}, \delta f_{Bias})$*. The minimum BFO goodness of fit,* GF_{BFO}*, occurs at longitude* $98.35°\,E$*. The figure shows only those points for which* $GF_{BFO} < 8$ *Hz. As the longitude increases from* $105°\,E$ *to* $107°\,E$*,* GF_{BFO} *increases from 8 to 40 Hz.*

altitude of 35,000 ft [7]. The radii of the small circles for this flight path range from 50% to 57% of the radius of the earth.

8. Discussion. The mathematical models developed by the Satellite Working Group (SWG) were based on the assumption that the flight path of MH370 was smooth after 19:41 UTC and that it conformed to the performance limitations for a Boeing 777 (*e.g.*, minimum and maximum speeds at a given altitude) [2]. With the SWG model, between ping times the aircraft was assumed to be traveling along a great circle at constant speed relative to the air. To determine the flight path from one ping arc to the next, the initial velocity of the aircraft was varied to minimize the error between the calculated and recorded BFO values [3]. This approach is similar to that taken in Model II. However, the SWG model also used meteorological data to incorporate the effect that winds had on the passage of the aircraft over the surface of the earth. The SWG verified their method by comparison with other flights in the same region on the same day, as well as with other flights of the same aircraft on the days immediately prior to the disappearance of MH370. The priority search area for MH370 that was announced by the ATSB on June 26th was based on the results obtained by the SWG. In Figure 7.2 (A), we show this search area with a thick black curve just below the 24:11 ping arc that extends from longitude 96°E to 101.5°E [2].

For the results presented in this paper, we used numerical optimization to determine the flight path that best fit the BTO and BFO data. To enrich the set of possible flight paths over which the optimization was performed, our model was based on segments of small circles rather than great circles. The results we obtained in Figure 7.2 (B) predict a very similar search area to that obtained by the ATSB [2]. This agreement between the two models—one based on wind-drifted great circles and the

other on small circles—is encouraging.

One of the main reasons for developing a mathematical model of a phenomenon is to use the model for prediction. To be useful, a model needs to capture the most salient aspects of the phenomenon and the equations in the model need to be solved with robust and accurate algorithms. Moreover, accurate input data is needed to make accurate predictions. In the case of the search for MH370 this data includes the initial position of the aircraft on one of the ping arcs and the frequency shifts δf_{AI} and δf_{Bias} in the BFO Equation (3.5). A recent refinement of this data by the Satellite Working Group [3] prompted the ATSB to shift the priority search area to a region on the final ping arc immediately southwest of the priority search area shown with the thick black curve in Figure 7.2.

9. Acknowledgements. I owe a great debt to the official Search Strategy Group coordinated by the Australian Transport Safety Bureau for releasing many details of their methods. Although the crash site of MH370 has not yet been found, the search would be hopeless without their efforts. I also learned much from the blog posts of Duncan Steel and his collaborators in the Independent Group. The manuscript was much improved thanks to the diligent work of two anonymous reviewers. Thanks also go to my Spring 2014 Multivariable Calculus class, and to Alan Boyle, Yanping Chen, Matthew Goeckner, Justin Jacobs, Brian Marks, Burkard Polster, Marty Ross, Yannan Shen, and my very supportive spouse and fellow mathematician Sue Minkoff.

REFERENCES

[1] C. Ashton, A. Shuster Bruce, G. Colledge, and M. Dickinson, The search for MH370, The Journal of Navigation, (2015), pp. 1–22.
[2] Australian Transport Safety Bureau, MH 370 - Definition of Underwater Search Areas, 26 June, 2014. http://www.atsb.gov.au/mh370/mh370-definition-of-underwater-search-areas.aspx (September 9, 2014).
[3] ———, MH 370 - Flight Path Analysis Update, 8 Oct, 2014. http://www.atsb.gov.au/media/5163181/AE-2014-054_MH370%20-FlightPathAnalysisUpdate.pdf (Oct 16, 2014).
[4] Inmarsat, MH370 Data Communications Logs, 2014. http://88.198.249.35/d/Inmarsat-Doppler-MH370.pdf (March 27, 2015).
[5] B. O'Neill, Elementary Differential Geometry, Academic Press, Waltham, Massachusetts, Second ed., 2006.
[6] Wikipedia, Aircraft Communications Addressing and Reporting System, 2014. http://en.wikipedia.org/wiki/Aircraft_Communications_Addressing_and_Reporting_System (September 29, 2014).
[7] ———, Boeing 777, 2014. http://en.wikipedia.org/wiki/Boeing_777 (September 29, 2014).
[8] ———, Earth's rotation, 2014. http://en.wikipedia.org/wiki/Earth's_rotation (September 9, 2014).
[9] ———, Geostationary orbit, 2014. http://en.wikipedia.org/wiki/Geostationary_orbit (September 9, 2014).
[10] ———, Malaysia Airlines Flight 370, 2014. http://en.wikipedia.org/wiki/Malaysia_Airlines_Flight_370 (September 9, 2014).
[11] ———, Analemma, 2015. http://en.wikipedia.org/wiki/Analemma (March 10, 2015).
[12] ———, Earth-centered inertial, 2015. http://en.wikipedia.org/wiki/Earth-centered_inertial (March 17, 2015).
[13] ———, ECEF, 2015. http://en.wikipedia.org/wiki/ECEF (March 17, 2015).
[14] J. Zweck, How did Inmarsat deduce possible flight paths for MH370?, SIAM News, 47 (2014), pp. 1,8. Also available online from http://www.siam.org/news/.

10. Appendix. In this Appendix, we outline solutions to some of the problems posed in the body of the paper.

Problem 2.1.1. We show that the constant speed great circle flight path, which at time, t_n, has position, $\mathbf{r}_n$, and velocity, $\mathbf{v}_n$, is parametrized by

$$\mathbf{r}_A(t) \;=\; \cos\left[\frac{v(t-t_n)}{R_A}\right]\mathbf{r}_n \;+\; \frac{R_A}{v}\sin\left[\frac{v(t-t_n)}{R_A}\right]\mathbf{v}_n, \tag{10.1}$$

where R_A is the radius of the sphere on which the great circle lies, and $v = |\mathbf{v}_n|$ is the speed of the aircraft.

Proof. Since the position vector, $\mathbf{r}_n$, is normal to the sphere and the velocity vector, $\mathbf{v}_n$, is tangent to the sphere, we have that $\mathbf{r}_n \perp \mathbf{v}_n$. Let $\mathbf{u}_n = \frac{R_A}{v}\mathbf{v}_n$. Then $\|\mathbf{r}_n\| = \|\mathbf{u}_n\| = R_A$. Let P be the plane centered at the origin with orthogonal basis $\{\mathbf{r}_n, \mathbf{u}_n\}$. The great circle lies in this plane. Then by vector algebra and trigonometry (draw a picture of the great circle in the plane P),

$$\mathbf{r}_A(t) \;=\; \cos[C(t-t_n)]\mathbf{r}_n + \sin[C(t-t_n)]\mathbf{u}_n, \tag{10.2}$$

for some constant C. To find C we calculate that $v = \|\mathbf{r}'_A(t)\| = R_A C$. □

Problem 2.1.3. Let $\mathbf{y}_\Theta$ and $\mathbf{y}_\Phi$ be unit vectors tangent to the coordinate curves, $\Phi = \Phi_n$ and $\Theta = \Theta_n$, respectively. Recall that the aircraft velocity at time t_n is

$$\mathbf{v}_n \;=\; v\cos\beta_n\,\mathbf{y}_\Theta \;+\; v\sin\beta_n\,\mathbf{y}_\Phi, \tag{10.3}$$

where the angle, β_n, is the heading direction of the aircraft. We will show that the ping arc equation,

$$\mathbf{r}_A(t_{n+1}) \;=\; R_A\mathbf{y}(\Theta_{n+1}, \Phi_{n+1}), \tag{10.4}$$

can be solved to obtain the formula for the heading direction given by

$$\sin\beta_n \;=\; \frac{\cos\left(\frac{v\Delta t_n}{R_A}\right)\cos\Phi_n \;-\; \cos\Phi_{n+1}}{\sin\left(\frac{v\Delta t_n}{R_A}\right)\sin\Phi_n}. \tag{10.5}$$

Proof. By Equation (10.1), the left hand side of the ping arc equation (10.4) is given by

$$\mathbf{r}_A(t_{n+1}) \;=\; \cos\left[\frac{v\Delta t_n}{R_A}\right]\mathbf{r}_n \;+\; \frac{R_A}{v}\sin\left[\frac{v\Delta t_n}{R_A}\right]\mathbf{v}_n, \tag{10.6}$$

where $\Delta t_n = t_{n+1} - t_n$. Recall that a satellite coordinate system is one for which the satellite is on the positive x-axis and the origin is at the center of the earth. Given any choice of satellite coordinate system, we can rotate it about the x-axis to obtain another satellite coordinate system which has the property that at time t_n the aircraft lies in the xy-plane, *i.e.*, $\Theta_n = 0$ (see Figure 2.1 (B)). With this choice of coordinates, by Equation (2.1), we have that

$$\mathbf{r}_n \;=\; R_A\mathbf{y}(0, \Phi_n) \;=\; R_A\left[\cos\Phi_n\mathbf{i}_S \;+\; \sin\Phi_n\mathbf{j}_S\right]. \tag{10.7}$$

Next we calculate $\mathbf{v}_n$ in terms of Φ_n and β_n. First, the vector $\mathbf{y}_\Theta$ is the unit vector in the direction of $\frac{\partial \mathbf{y}}{\partial \Theta}$ and $\mathbf{y}_\Phi$ is the unit vector in the direction of $\frac{\partial \mathbf{y}}{\partial \Phi}$. Therefore,

$$\mathbf{y}_\Phi = -\sin\Phi\,\mathbf{i}_S + \cos\Theta\cos\Phi\,\mathbf{j}_S + \sin\Theta\cos\Phi\,\mathbf{k}_S, \tag{10.8}$$

$$\mathbf{y}_\Theta = -\sin\Theta\,\mathbf{j}_S + \cos\Theta\,\mathbf{k}_S. \tag{10.9}$$

Substituting these expressions into Equation (10.3) and using $\Theta_n = 0$, we obtain

$$\mathbf{v}_n = -v\sin\beta_n\sin\Phi_n\,\mathbf{i}_S + v\sin\beta_n\cos\Phi_n\,\mathbf{j}_S + v\cos\beta_n\,\mathbf{k}_S. \tag{10.10}$$

Substituting Equations (10.7) and (10.10) into Equation (10.6) we obtain an expression for the left-hand side, $\mathbf{r}_A(t_{n+1})$, of the ping arc equation (10.4) in terms of Φ_n and β_n. Next, we observe that by Equation (2.1), the $\mathbf{i}_S$-component of the right-hand side of the ping arc equation is the only component that is independent of the unknown angle, Θ_{n+1}. Therefore, to solve for β_n, we take the inner product of Equation (10.4) with $\mathbf{i}_S$. After an algebraic manipulation, we obtain the required Equation (10.5). □

Problem 3.1.1. We show that for a geostationary satellite, the aircraft-satellite Doppler shift, Δf_n, at the n-th ping arc is related to the component, $v_{\Phi,n}$, of the aircraft velocity that is perpendicular to the ping arc by

$$\Delta f_n = -\frac{f}{c}\frac{R_S}{D_{\mathrm{SA},n}}\,v_{\Phi,n}\sin\Phi_n, \tag{10.11}$$

where Φ_n is the ping arc angle and the distance, $D_{\mathrm{SA},n}$, between the satellite and aircraft is

$$D_{\mathrm{SA},n} = \sqrt{R_S^2 - 2R_SR_A\cos\Phi_n + R_A^2}. \tag{10.12}$$

Proof. Since $\{\mathbf{y}_n, \mathbf{y}_{\Phi,n}, \mathbf{y}_{\Theta,n}\}$ is an orthonormal basis,

$$\widehat{\mathbf{u}}(t_n)\cdot\mathbf{y}_{\Theta,n} = \frac{[\mathbf{r}_A(t_n)-\mathbf{r}_S]\cdot\mathbf{y}_{\Theta,n}}{\|\mathbf{r}_A(t_n)-\mathbf{r}_S\|} = \frac{[R_A\mathbf{y}_n - R_S\mathbf{i}_S]\cdot\mathbf{y}_{\Theta,n}}{D_{\mathrm{SA},n}} = 0, \tag{10.13}$$

since, by Equation (10.9), the $\mathbf{i}_S$-component of $\mathbf{y}_{\Theta,n}$ is zero. Therefore, by Equations (3.1), (3.2) and (10.8),

$$\Delta f_n = -\frac{f}{c}\frac{1}{D_{\mathrm{SA},n}}\,[R_A\mathbf{y}_n - R_S\mathbf{i}_S]\cdot[v_{\Theta,n}\mathbf{y}_{\Theta,n} + v_{\Phi,n}\mathbf{y}_{\Phi,n}] = -\frac{f}{c}\frac{R_S}{D_{\mathrm{SA},n}}\,v_{\Phi,n}\sin\Phi_n, \tag{10.14}$$

as required. □

Problem 4.1.3. Let

$$R_S(t) = \overline{R}_S[1+\epsilon_S\sin(\alpha(t-t_0))], \tag{10.15}$$

$$v_S(t) = \overline{v}_S[1-\epsilon_S\sin(\alpha(t-t_0))]. \tag{10.16}$$

We show that if

$$\mathbf{r}_S(t) = R_S(t)\left[\cos\theta_S(t)\,\mathbf{i}_P + \sin\theta_S(t)\,\mathbf{j}_P\right], \tag{10.17}$$

where

$$\theta_S(t) = \frac{\pi}{2} + \int_{t_0}^{t}\frac{v_S(s)}{R_S(s)}\,ds, \tag{10.18}$$

then

$$\theta_S(t) \;\approx\; \frac{\pi}{2} + \alpha(t-t_0) + 2\epsilon_S\left\{\cos[\alpha(t-t_0)] - 1\right\} + \mathcal{O}(\epsilon_S^2), \tag{10.19}$$

and

$$\|\mathbf{r}'_S(t)\| = v_S(t) + \mathcal{O}(\epsilon_S^2). \tag{10.20}$$

Proof. Substituting Equations (10.15) and (10.16) into Equation (10.18) and using the fact that $\overline{v}_S = \alpha\overline{R}_S$, we find that

$$\theta_S(t) \;=\; \frac{\pi}{2} \;+\; \alpha\int_0^{t-t_0} 1 - \frac{2\epsilon_S\sin\alpha s}{1+\epsilon_S\sin\alpha s}\,ds \tag{10.21}$$

$$\;=\; \frac{\pi}{2} \;+\; \alpha(t-t_0) - 2\epsilon_S\alpha\int_0^{t-t_0}\sin\alpha s\,ds \;+\; \mathcal{O}(\epsilon_S^2) \tag{10.22}$$

$$\;=\; \frac{\pi}{2} + \alpha(t-t_0) + 2\left\{\cos[\alpha(t-t_0)] - 1\right\} + \mathcal{O}(\epsilon_S^2), \tag{10.23}$$

as required.

Next, to prove Equation (10.20), we use (10.15) and (10.16) to show that

$$\mathbf{r}'_S(t) \;=\; [R'_S(t)\cos\theta_S(t) - v_S(t)\sin\theta_S(t)]\,\mathbf{i}_P \;+\; [R'_S(t)\sin\theta_S(t) + v_S(t)\cos\theta_S(t)]\,\mathbf{j}_P. \tag{10.24}$$

Therefore,

$$\|\mathbf{r}'_S(t)\|^2 \;=\; [R'_S(t)]^2 \;+\; [v_S(t)]^2 \;=\; \overline{v}_S^2\left\{1 - 2\epsilon_S\sin[\alpha(t-t_0)] + \epsilon_S^2\right\}, \tag{10.25}$$

and so

$$\|\mathbf{r}'_S(t)\| \;=\; \overline{v}_S\left\{1 - 2\epsilon_S\sin[\alpha(t-t_0)] + \epsilon_S^2\right\}^{1/2} \tag{10.26}$$

$$\;=\; \overline{v}_S\left\{1 + \tfrac{1}{2}(-2\epsilon_S\sin[\alpha(t-t_0)] + \epsilon_S^2)\right\} + \mathcal{O}(\epsilon_S^2) \tag{10.27}$$

$$\;=\; v_S(t) + \mathcal{O}(\epsilon_S^2), \tag{10.28}$$

as required. □

Problem 4.1.4. We show that if

$$\mathbf{r}_S(t) \;=\; R_S(t)\,\mathbf{R}(\theta_P - \alpha t, \phi_P)\,[\mathbf{R}(\theta_S(t))]_{*1}, \tag{10.29}$$

then

$$\mathbf{i}_S(t) \;:=\; \frac{\mathbf{r}_S(t)}{R_S(t)} \;=\; \begin{bmatrix} -\delta_C\cos[\theta_S(t) + \alpha t - \theta_P] + (1-\delta_C)\cos[\theta_S(t) - \alpha t + \theta_P] \\ \delta_C\sin[\theta_S(t) + \alpha t - \theta_P] + (1-\delta_C)\sin[\theta_S(t) - \alpha t + \theta_P] \\ -\delta_S\cos\theta_S(t) \end{bmatrix}, \tag{10.30}$$

where $\delta_C = \frac{1}{2}(1-\cos\phi_P)$ and $\delta_S = \sin\phi_P$, and that

$$\mathbf{j}_S(t) \;=\; \frac{d}{d\theta_S}\mathbf{i}_S(t) \;=\; \begin{bmatrix} \delta_C\sin[\theta_S(t) + \alpha t - \theta_P] - (1-\delta_C)\sin[\theta_S(t) - \alpha t + \theta_P] \\ \delta_C\cos[\theta_S(t) + \alpha t - \theta_P] + (1-\delta_C)\cos[\theta_S(t) - \alpha t + \theta_P] \\ \delta_S\sin\theta_S(t) \end{bmatrix}. \tag{10.31}$$

Proof. Let $\theta_1 = \theta_P - \alpha t$ and $\theta_2 = \theta_S(t)$. Then by (10.29),

$$\begin{aligned}
\mathbf{i}_S(t) &= \mathbf{R}(\theta_P - \alpha t, \phi_P)\,[\mathbf{R}(\theta_S(t))]_{*1} \\
&= \begin{bmatrix} \cos\theta_1\cos\theta_2\cos\phi_P - \sin\theta_1\sin\theta_2 \\ \sin\theta_1\cos\theta_2\cos\phi_P + \cos\theta_1\sin\theta_2 \\ -\sin\phi_P\cos\theta_2 \end{bmatrix} \\
&= \begin{bmatrix} \frac{1}{2}\{[\cos(\theta_1+\theta_2)+\cos(\theta_1-\theta_2)]\cos\phi_P + [\cos(\theta_1+\theta_2)-\cos(\theta_1-\theta_2)]\} \\ \frac{1}{2}\{[\sin(\theta_1+\theta_2)+\sin(\theta_1-\theta_2)]\cos\phi_P + [\sin(\theta_1+\theta_2)-\sin(\theta_1-\theta_2)]\} \\ -\sin\phi_P\cos\theta_2 \end{bmatrix} \\
&= \begin{bmatrix} -\delta_C\cos[\theta_S(t)+\alpha t-\theta_P] + (1-\delta_C)\cos[\theta_S(t)-\alpha t+\theta_P] \\ \delta_C\sin[\theta_S(t)+\alpha t-\theta_P] + (1-\delta_C)\sin[\theta_S(t)-\alpha t+\theta_P] \\ -\delta_S\cos\theta_S(t) \end{bmatrix},
\end{aligned}$$

as required. To show that $\mathbf{j}_S(t) = \frac{d}{d\theta_S}\mathbf{i}_S(t)$ we recall from Equation (4.13) that

$$\begin{bmatrix}\mathbf{i}_S(t) & \mathbf{j}_S(t) & \mathbf{k}_S(t)\end{bmatrix} = \mathbf{R}(\theta_P - \alpha t, \phi_P)\,\mathbf{R}(\theta_S(t)). \tag{10.32}$$

So by linearity of the derivative and of matrix multiplication,

$$\frac{d}{d\theta_S}\begin{bmatrix}\mathbf{i}_S & \mathbf{j}_S & \mathbf{k}_S\end{bmatrix} \tag{10.33}$$

$$= \mathbf{R}(\theta_P - \alpha t, \phi_P)\,\frac{d}{d\theta_S}\mathbf{R}(\theta_S) \tag{10.34}$$

$$= \mathbf{R}(\theta_P - \alpha t, \phi_P)\,\frac{d}{d\theta_S}\begin{bmatrix}\cos\theta_S & -\sin\theta_S & 0 \\ \sin\theta_S & \cos\theta_S & 0 \\ 0 & 0 & 1\end{bmatrix}. \tag{10.35}$$

The required result now follows from the fact that the θ-derivative of the first column of the rotation matrix $\mathbf{R}(\theta)$ equals the second column of $\mathbf{R}(\theta)$. □

Problem 5.1.1. We show that the position of the aircraft at time t_{n+1} is given by

$$\mathbf{r}_{n+1} = R_A\mathbf{F}_n\mathbf{Y}_n\mathbf{x}_n, \tag{10.36}$$

where $\mathbf{x}_n = \mathbf{x}_n(v_{\Phi,n}, v_{\Theta,n})$ is the unit column vector defined by

$$\mathbf{x}_n = \frac{1}{v_n}\begin{bmatrix}v_n\cos(v_n\Delta t_n/R_A) & v_{\Phi,n}\sin(v_n\Delta t_n/R_A) & v_{\Theta,n}\sin(v_n\Delta t_n/R_A)\end{bmatrix}^T. \tag{10.37}$$

Here $v_n = \sqrt{v_{\Phi,n}^2 + v_{\Theta,n}^2}$ and $\Delta t_n = t_{n+1} - t_n$. We show that the **vector ping arc equation** which enforces the condition that the aircraft cross the $(n+1)$-st ping arc at time t_{n+1}, is given by

$$\mathbf{x}_n = \mathbf{A}_n\mathbf{y}_{n+1}, \qquad \text{where } \mathbf{A}_n = \mathbf{Y}_n^T\mathbf{F}_n^T\mathbf{F}_{n+1} \text{ is orthogonal,} \tag{10.38}$$

and that we can eliminate Θ_{n+1} from Equation (10.38) to obtain the **scalar ping arc equation**

$$f_{\text{Ping}}(v_{\Phi,n}, v_{\Theta,n}) := R_A\{(\mathbf{x}_n)_1 - a - \mathbf{b}^T\mathbf{x}_n\} = 0, \tag{10.39}$$

where $a = (\mathbf{A}_n)_{11}\cos\Phi_{n+1}$ and $\mathbf{b}^T = (\mathbf{A}_n)_{12}(\mathbf{A}_n^T)_{2*} + (\mathbf{A}_n)_{13}(\mathbf{A}_n^T)_{3*}$.

Proof. By Equation (2.3), the expressions for $\mathbf{r}_n$ and $\mathbf{v}_n$ given in and above Equation (5.4), and by Lemma 4.1,

$$\begin{aligned}\mathbf{r}_{n+1} &= \cos(v_n\Delta t_n/R_A)\,\mathbf{r}_n + \frac{R_A}{v_n}\sin(v_n\Delta t_n/R_A)\,\mathbf{v}_n,\\ &= R_A\mathbf{F}_n\left\{\cos(v_n\Delta t_n/R_A)(\mathbf{Y}_n)_{*1} + \frac{1}{v_n}\sin(v_n\Delta t_n/R_A)\begin{bmatrix}(\mathbf{Y}_n)_{*2} & (\mathbf{Y}_n)_{*3}\end{bmatrix}\begin{bmatrix}v_{\Phi,n}\\ v_{\Theta,n}\end{bmatrix}\right\}\\ &= R_A\mathbf{F}_n\mathbf{Y}_n\mathbf{x}_n,\end{aligned}$$

as required. Since the condition that the aircraft cross the $(n+1)$-st ping arc at time t_{n+1} can be expressed as $\mathbf{r}_{n+1} = R_A\mathbf{F}_{n+1}\mathbf{y}_{n+1}$, we have that $\mathbf{F}_n\mathbf{Y}_n\mathbf{x}_n = \mathbf{F}_{n+1}\mathbf{y}_{n+1}$. Since all matrices in this equation are orthogonal, multiplying on the left by $(\mathbf{F}_n\mathbf{Y}_n)^T$ yields (10.38) as required.

To derive Equation (10.39), we observe that by Equations (5.2) and (10.38)

$$\begin{bmatrix}\cos\Phi_{n+1}\\ \cos\Theta_{n+1}\sin\Phi_{n+1}\\ \sin\Theta_{n+1}\sin\Phi_{n+1}\end{bmatrix} = (\mathbf{Y}_{n+1})_{*1} = \mathbf{y}_{n+1} = \begin{bmatrix}(\mathbf{A}_n^T)_{1*}\mathbf{x}_n\\ (\mathbf{A}_n^T)_{2*}\mathbf{x}_n\\ (\mathbf{A}_n^T)_{3*}\mathbf{x}_n\end{bmatrix}. \tag{10.40}$$

On the other hand, also by (10.38), $(\mathbf{x}_n)_1 = (\mathbf{A}_n)_{1*}\mathbf{y}_{n+1}$. To eliminate Θ_{n+1} from this equation, we use the right hand side of (10.40) to obtain

$$\begin{aligned}(\mathbf{x}_n)_1 &= (\mathbf{A}_n)_{11}(\mathbf{y}_{n+1})_1 + (\mathbf{A}_n)_{12}(\mathbf{y}_{n+1})_2 + (\mathbf{A}_n)_{13}(\mathbf{y}_{n+1})_3\\ &= (\mathbf{A}_n)_{11}\cos\Phi_{n+1} + [(\mathbf{A}_n)_{12}(\mathbf{A}_n^T)_{2*} + (\mathbf{A}_n)_{13}(\mathbf{A}_n^T)_{3*}]\mathbf{x}_n,\end{aligned}$$

as required. □

Problem 5.1.2. The **second Doppler shift equation** is given by

$$f_{\text{Doppler},2}(v_{\Phi,n}, v_{\Theta,n}) = \Delta f_{n+1} - g(v_{\Phi,n}, v_{\Theta,n}) = 0, \tag{10.41}$$

where, arguing as in the first Doppler shift equation (5.3),

$$\begin{aligned}g(v_{\Phi,n}, v_{\Theta,n}) =\\ &\frac{f}{cD_{\text{SA},n+1}}\left[-v_{\Phi,n+1}R_{S,n+1}\sin\Phi_{n+1} - (R_{S,n+1} - R_A\cos\Phi_{n+1})(\mathbf{v}_{S,n+1})_1\right.\\ &\left. + R_A\cos\Theta_{n+1}\sin\Phi_{n+1}(\mathbf{v}_{S,n+1})_2 + R_A\sin\Theta_{n+1}\sin\Phi_{n+1}(\mathbf{v}_{S,n+1})_3\right].\end{aligned} \tag{10.42}$$

However because we do not know $v_{\Phi,n+1}$ and Θ_{n+1}, we need to express them in terms of $(v_{\Phi,n}, v_{\Theta,n})$. First, by Equation (10.40), Θ_{n+1} is given in terms of $(v_{\Phi,n}, v_{\Theta,n})$ by

$$\begin{bmatrix}\cos\Theta_{n+1} & \sin\Theta_{n+1}\end{bmatrix} = \begin{bmatrix}(\mathbf{A}_n^T)_{2*}\mathbf{x}_n & (\mathbf{A}_n^T)_{3*}\mathbf{x}_n\end{bmatrix}, \tag{10.43}$$

where $\mathbf{x}_n(v_{\Phi,n}, v_{\Theta,n})$ is given by Equation (10.37). Finally, using Equations (2.3) and (5.4), the definition of $\mathbf{A}$ given in Equation (5.7), and Lemma 4.1 it follows that $v_{\Phi,n+1}$ is given in terms of $(v_{\Phi,n}, v_{\Theta,n})$ by

$$v_{\Phi,n+1} = v_n(\mathbf{Y}_{n+1}^T\mathbf{A}_n^T)_{2*}\mathbf{u}_n, \tag{10.44}$$

where $\mathbf{Y}_{n+1} = \mathbf{Y}_{n+1}(\Theta_{n+1}, \Phi_{n+1})$ is given as in Equation (5.2) and

$$\mathbf{u}_n = \frac{1}{v_n}\begin{bmatrix}-v_n\sin(v_n\Delta t_n/R_A) & v_{\Phi,n}\cos(v_n\Delta t_n/R_A) & v_{\Theta,n}\cos(v_n\Delta t_n/R_A)\end{bmatrix}^T. \tag{10.45}$$

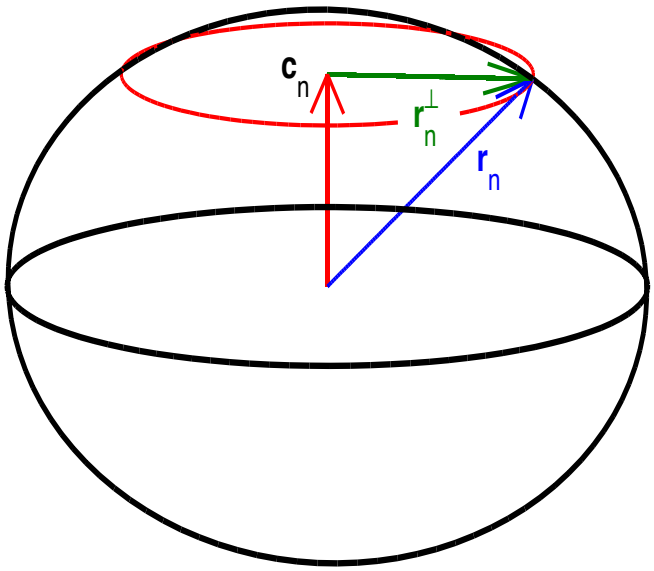

FIG. 10.1 *Sketch showing the vectors in the small circle parametrization* (10.46).

Problem 6.1.1. We show that the parametrization of the small circle of geodesic curvature, κ_g, that lies on the sphere of radius, R_A, and which at time, t_n, has position, $\mathbf{r}_n$, and velocity, $\mathbf{v}_n$, is given by

$$\mathbf{r}(t) \;=\; \mathbf{c} \;+\; \cos\left[\frac{v(t-t_n)}{R_C}\right]\mathbf{r}_n^{\perp} \;+\; \frac{R_C}{v}\sin\left[\frac{v(t-t_n)}{R_C}\right]\mathbf{v}_n, \tag{10.46}$$

where $\mathbf{c}$ is the center and R_C is the radius of the small circle, $\mathbf{r}_n^{\perp} = \mathbf{r}_n - \mathbf{c}$ and $v = |\mathbf{v}_n|$. Furthermore, if we let $\mathbf{w}_n = \frac{\mathbf{r}_n}{R_A} \times \frac{\mathbf{v}_n}{v}$, then $\mathcal{C} = \{\frac{\mathbf{r}_n}{R_A}, \frac{\mathbf{v}_n}{v}, \mathbf{w}_n\}$ is a frame at $\mathbf{r}_n$ adapted to the small circle, and

$$\frac{\mathbf{r}(t)}{R_A} \;=\; \left[1 + \frac{\cos\alpha_n(t) - 1}{1+K^2}\right]\frac{\mathbf{r}_n}{R_A} \;+\; \frac{K(\cos\alpha_n(t)-1)}{1+K^2}\,\mathbf{w}_n \;+\; \frac{\sin\alpha_n(t)}{\sqrt{1+K^2}}\,\frac{\mathbf{v}_n}{v}, \tag{10.47}$$

where $K = R_A\kappa_g/v$ and $\alpha_n(t) = v(t-t_n)/R_C$.

Proof. By Figure 10.1, we see that $\mathbf{r}_n^{\perp}$ is a radial vector to the small circle, C, with $\|\mathbf{r}_n^{\perp}\| = R_C$, and that $\mathbf{v}_n$ is a tangent vector to C at $\mathbf{r}_n$. Furthermore, $\mathbf{r}_n^{\perp} \perp \mathbf{v}_n$ as $\mathbf{v}_n \cdot \mathbf{r}_n^{\perp} = \mathbf{v}_n \cdot \mathbf{r}_n - \mathbf{v}_n \cdot \mathbf{c} = 0$, since on the one hand $\mathbf{r}_n$ is normal and $\mathbf{v}_n$ is tangent to the sphere, and on the other hand $\mathbf{c}$ is normal and $\mathbf{v}_n$ is tangent to the plane in which C lies. Equation (10.46) now follows by arguing as we did in the proof of Equation 10.1 above.

To prove Equation (10.47), we first express $\mathbf{r}_n^{\perp}$ in the frame $\mathcal{C}$ as

$$\mathbf{r}_n^{\perp} \;=\; R_C\left[\cos\gamma\,\frac{\mathbf{r}_n}{R_A} \;+\; \sin\gamma\,\mathbf{w}_n\right], \tag{10.48}$$

for some angle, γ. Here we have used the facts that $\mathbf{r}_n^\perp \perp \mathbf{v}_n$ and $\|\mathbf{r}_n^\perp\| = R_C$. To determine the angle γ, we observe that the vector $\mathbf{r}_n - 2\mathbf{r}_n^\perp$ lies on the sphere (see Figure 10.1), so that

$$R_A^2 \;=\; \|\mathbf{r}_n - 2\mathbf{r}_n^\perp\|^2 \;=\; R_A^2\left(1 - \frac{2R_C}{R_A}\cos\gamma\right)^2 + (2R_C\sin\gamma)^2. \tag{10.49}$$

Consequently

$$\cos\gamma \;=\; \frac{R_C}{R_A} \;=\; \frac{1}{\sqrt{1+K^2}} \qquad \text{and} \qquad \sin\gamma \;=\; \frac{K}{\sqrt{1+K^2}}, \tag{10.50}$$

by Equation (6.1). An algebraic calculation then yields Equation (10.47). □